CrossMark

ORIGINAL PAPER

Experimental and numerical studies on the performance and surface streamlines on the blades of a horizontal-axis wind turbine

Chi-Jeng Bai[1] · Wei-Cheng Wang[2] · Po-Wei Chen[2]

Abstract Investigating laminar separation over the turbine blade of a horizontal-axis wind turbine (HAWT) has been considered an important task to improve the aerodynamic performance of a wind turbine. To better understand the laminar separation phenomena, in this study, the aerodynamic forces of a SD8000 airfoil (representing the sectional blade shape) in the steady-state conditions were first predicted using an incompressible Reynolds-averaged Navier–Stokes solver with the γ–$Re_{\theta t}$ and k–k_L–ω transition models. By comparing simulation and experimental results, the k–k_L–ω transition model was chosen to simulate the laminar separation on three-dimensional (3D) turbine blade. Experimentally, a HAWT with three blades was then tested in a close-circuit wind tunnel between the tip speed ratios (TSRs) of 2 and 7 at the wind speed of 10 m/s. In addition, through computational fluid dynamics, the turbine performance and flow characteristics on the blade as blade is rotating were investigated. It is shown that 3D simulations agreed well with the experimental results with regard to the mechanical power of the HAWT at the testing TSRs. Moreover, the separation and reattachment lines on the suction surface of the turbine blade were also observed through the skin friction line, indicating that laminar separation moved toward the trailing edge with the increasing TSR at the blade tip region.

Introduction

Wind energy has been considered as one of the most promising renewable energy sources. Recently, focus has been placed on the small-scale horizontal-axis wind turbine (HAWT) with low Reynolds numbers due to its potential for residential electricity generation. In order to have the optimal power output from the wind turbine system, it is necessary to improve on the design of turbine blade and examine the aerodynamic performance of the blade. Small-scale wind turbines operating at low Reynolds numbers suffer from laminar separation bubbles (LSBs) due to their blade size or low wind speeds.

LSB is a flow phenomenon occurred at low Reynolds numbers between 50,000 and 200,000 has and have been shown to exhibit negative effects to aerodynamic performance (Lian and Shyy 2007; Swanson and Isaac 2010), such as decrease of lift force, increase of drag force, vibration, and noise experimentally observed on the two-dimensional (2D) airfoil. The formation of LSB results from the strong adverse pressure gradient, making the laminar boundary layer separate from the airfoil surface. Many flow control techniques, such as turbulators, plasma actuators (Huang et al. 2006), and Gurney flaps (Byerley et al. 2003), have been applied to prevent the occurrence of separation. LSB may occur on the blades of small HAWTs since they operate at low Reynolds number region. The turbine performance would be severely affected because of the reduction in lift-to-drag (L/D) ratio. In addition,

✉ Wei-Cheng Wang
 wilsonwang@mail.ncku.edu.tw

1 Wind Power Technology Center, China Steel Corporation, No. 1, Chung Kang Rd., Hsiao Kang, Kao-Hsiung 81233, Taiwan

2 Department of Aeronautics and Astronautics, National Cheng Kung University, Tainan 70101, Taiwan

observing the LSB phenomenon is relatively difficult due to the rotation of the turbine blade. It is hence important to improve our understanding of laminar separation on the HAWT blades.

The LSB phenomenon has been studied experimentally (O'Meara and Mueller 1987) and numerically on 2D airfoil. The flow along the boundary layer separates due to an adverse pressure gradient of sufficient magnitude (Schlichting and Gersten 2003). Observing and summarizing the positions of separation and reattachment points and the thickness of the bubble for this flow phenomenon using experimental methods in different Reynolds numbers and airfoil types were the main research direction. O'Meara and Mueller (1987) found that the LSB on NACA66$_3$-018 airfoil decreased in length and thickness as the Reynolds number was increased, and that a linear relationship existed between the bubble thickness and the total bubble length. Genç et al. (2012) and Sharma and Poddar (2010) observed the LSB and the transition process on NACA2414 and NACA0015 airfoils. They concluded that the separation point moved towards the leading edge of the airfoils as the angle of attack increased.

Recently, computational fluid dynamics (CFDs) approach has been widely applied for investigating low Reynolds number aerodynamic characteristics. For example, direct numerical simulation approach has been used for investigating the LSB phenomenon on the upper surface of an airfoil (Rist and Maucher 2002; Shan et al. 2005; Sharma and Poddar 2010; Singh and Sarkar 2011), which captures the details of flow separation, detached shear layer, vortex shedding, and reattachment of the boundary layer. In addition, Reynolds-averaged Navier–Stokes (RANS) simulations are popular to predict cases with relatively complex geometries and flows. The k–ε and k–ω turbulence models have been applied to various industries, including renewable energy, environment, and aerospace (Bassi et al. 2005; Menter 1994; Richards and Hoxey 1993; Shih et al. 1995; Stapleton et al. 2000). The flow fields in these applications can be laminar, transition or turbulent. To obtain the accurate flow structure in the region of transition, appropriate simulation model has to be selected.

Transition models have been developed, such as γ–$Re_{\theta t}$ transition and k–k_L–ω transition models. The γ–$Re_{\theta t}$ transition model is based on k–ω SST transport equations linked with two additional transport equations: One is for the intermittency γ and the other one is for the transition Reynolds number $Re_{\theta t}$ (Menter et al. 2004; Malan and Suluksna 2009). It is difficult to compute the general three-dimensional (3D) flows, such as a turbine blade sidewall boundary layer. The k–k_L–ω transition model is based on the solution of three additional transport equations, turbulent kinetic energy (k), laminar kinetic energy (k_L), and turbulent specific dissipation (ω), as described by Walters and Leylek (2004). This model has been successfully implemented the investigations of LSB. The positions of separation and reattachment points were observed on NACA2415 airfoil between the angles of attack of $-10°$ and $20°$ at Reynolds numbers of 0.5×10^5–3.0×10^5 (Genç et al. 2009, 2011, 2012). As angle of attack increased, the points of separation and transition moved to the leading edge. As Reynolds number decreased, short bubble breaks at higher angles of attack and this results in long bubble to occur (Genç et al. 2012). In these studies, both k–k_L–ω and k–ω SST transition models accurately predict the location of separation bubble (Genç et al. 2009).

CFD technique has also been applied to visualize the flow structure around the blade of wind turbines. Digraskar (2010) carried out the flow visualization using CFD with the k–ω SST and Spalart–Allmaras turbulence models over the NREL Phase VI wind turbine rotor in which the sectional blade shape of the turbine blade consists of NREL S809 airfoil. Bechmann et al. (2011) also carried out CFD investigation using RANS method on MEXICO rotor blade, which consists of DU91-W2-250, RISOE A21, and NACA64418 airfoils along its blade section. Langtry et al. (2006) developed a correlation-based transition model based on two transport equations to validate the model for predicting transition on wind turbines. The fully turbulent and transitional computation of both 2D S809 airfoil and 3D wind turbine rotor were successfully simulated. Pape and Lecanu (2004) observed the flow field around the turbine blade using the compressible *els*A Navier–Stokes solver, showing that the 3D flow field has massive flow separation around the turbine blade due to the radial centrifugal force. Previous studies indicated that as the Reynolds numbers are within the transition region, LSB occurs on 2D airfoils, the main component of turbine blade. Studying the laminar separation on a rotating HAWT blade becomes significant for improving the aerodynamic performance of HAWTs.

In this study, firstly, 2D simulations of the flow around a SD8000 airfoil are performed using the k–ω SST and the γ–$Re_{\theta t}$ models. The results were compared with experimental data for validation purposes. The lift and drag coefficients between the angles of attack of $-6°$ and $20°$ were examined at the Reynolds number of 1×10^5. The agreement of 2D simulation and experimental data leads to the selection of the transition model for 3D simulation. Then, an untwisted and untapered HAWT with three blades was tested in a closed circuit wind tunnel for measuring the mechanical power output at wind speed of 10 m/s. The 3D simulation was validated by comparing the results with wind tunnel experiment, and this allowed us to examine the flow structure around the turbine blade and investigate the laminar separation phenomenon.

Methods

Experimental set up

The experiment was performed in a closed-circuit wind tunnel with two test sections which belong to the Architecture and Building Research Institute in Taiwan. The test section is 36.5 m long and the cross-section dimensions are 4.0 m wide $\times$ 3.6 m high. The rotor blockage ratio, defined as A_b/A_w, was 5.5 %, i.e., less than the 10 % limit (Spera 1994). Figure 1 (left) shows the HAWT system inside the wind tunnel test section.

Test model

In order to validate the 3D simulation, a baseline variable-speed HAWT with three blades was tested in the wind tunnel described above. The blades were made of engineering plastic, acrylonitrile–butadiene–styrene, and the blade profile was the SD8000 airfoil. The radius of blade and the chord length are 0.50 and 0.09 m, respectively. The pitch angle of the blade is set to be 0°.

Measurement equipment

A pitot-static tube was installed upstream of the wind turbine in order to measure the free stream velocity. The maximum wind speed of the wind tunnel was 30 m/s, and the turbulence intensity was less than 0.35 % between wind speeds of 5 and 15 m/s.

A torque sensor was mounted on the main shaft between the turbine and the generator in order to measure the mechanical torque, as shown in Fig. 2 (right). This technique has been applied by many researchers. (Hirahara et al. 2005; Hsiao et al. 2013; Kang and Meneveau 2010). In order to
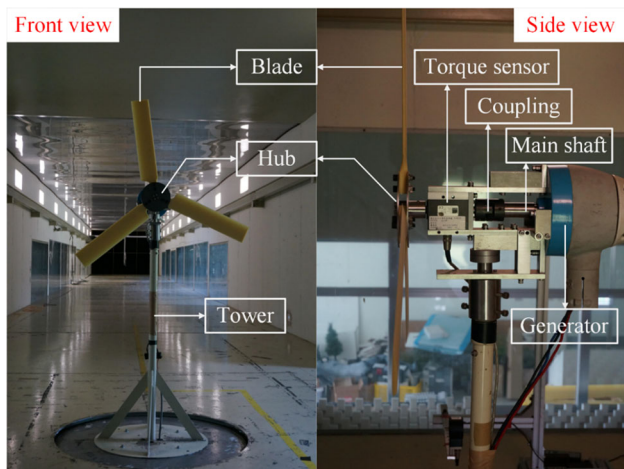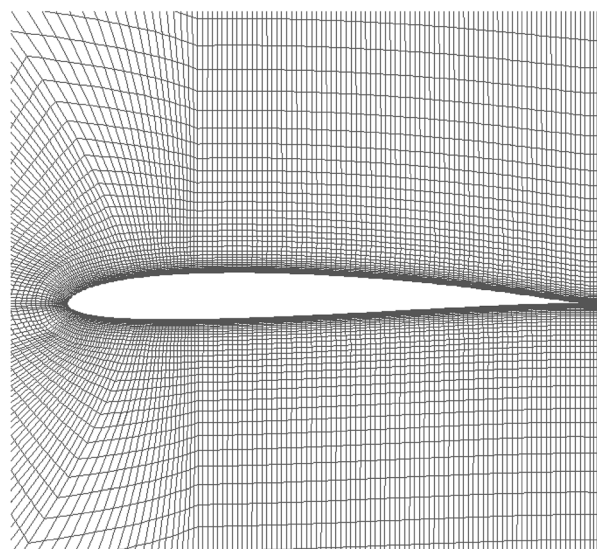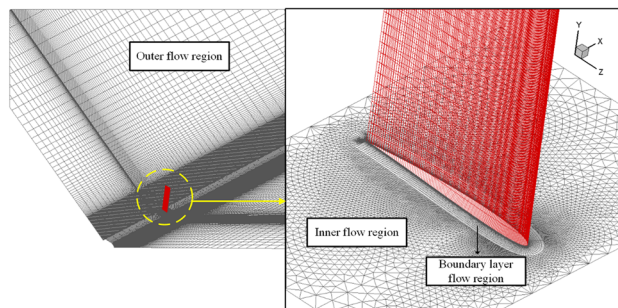

(a)

(b)

Fig. 2 The mesh domains for **a** 2D SD8000 airfoil, and **b** 3D HAWT blade

acquire the values of mechanical torque at various rotational speeds, a high-current DC electronic load module (DCELM) was used. If the circuit load is adjusted by the DCELM, the rotational speed of the turbine blade will also be changed. Therefore, the signals of rotational speed for the turbine blade need to be detected by the proximity switch. Only the DC signal was analyzed in this experiment, and a diode bridge circuit was used to convert the AC to fluctuating DC.

The data acquisition in voltage outputs from these sensors was taken care of by National Instrument (NI) USB-6008 12 bit AD converter, and the data including mechanical torques, voltages, currents, wind speeds, and rotational speeds were measured and collected using NI LabView. The mechanical power and power coefficients were then calculated based on the measured data.

Experimental conditions

Torque and thrust of the turbine blade were integrated by the lift and drag forces on the blade sections. The lift and drag are available as functions of the angles of attack and

Fig. 1 The aerodynamic performance measurements on HAWT system inside the wind tunnel test section

the local Reynolds numbers (Re_L, the Reynolds number at each blade section), which are defined as

$$Re_L = \frac{c_{avg} V_{rel} \rho}{\mu}, \quad (1)$$

where c_{avg} is the average chord length of each blade section, ρ is the air density, μ is the absolute viscosity, and V_{rel} is the relative wind speed which consists of wind speed (V) and rotational speed (ω). In addition, the V_{rel} includes the effects of axial (a) and angular (a') induction factors represented as

$$V_{rel} = \sqrt{[V(1-a)]^2 + [R\omega(1+a')]^2}. \quad (2)$$

The rotational speed has a relationship between the radius of blade (R) and the wind speed called tip speed ratio (TSR):

$$TSR = \frac{R\omega}{V}. \quad (3)$$

The local Reynolds numbers with different TSRs are calculated based on the procedures described in authors' previous studies (Bai et al. 2014, 2016) using $c_{avg} = 0.09$ m, $V = 10$ m/s, $\rho = 1.225$ kg/m^3, $\mu = 1.79 \times 10^{-5}$ Pa s, and $R = 0.50$ m, and the TSR is chosen between 2 to 7. Table 1 shows the average Reynolds numbers (Re_{ave}, the Reynolds number for the entire blade) determined under these conditions.

Numerical approach

In this study, an incompressible Navier–Stokes solver was applied to predict the aerodynamic characteristics of a 2D SD8000 airfoil and a 3D baseline HAWT blade of the same profile. All 2D and 3D simulations were performed via the commercial software FLUENT^{TM}, and the second-order upwind spatial discretization was used. The resulting system of equations was solved using the SIMPLE coupled solution. The convergence criterion was satisfied to be below 10^{-10} in all dependent variable residuals.

Table 1 Reynolds number distributions between the tip speed of 2 and 7 at wind speed of 10 m/s

Tip speed ratios	Average Reynolds numbers
2	66,359
3	71,852
4	78,903
5	87,133
6	96,242
7	106,003

For the 2D simulation, the γ–$Re_{\theta t}$ transition model (Malan and Suluksna 2009) and k–k_L–ω transition model (Walters and Leylek 2004) were used at the Reynolds number of 1×10^5 and the angles of attack between $-6°$ and $20°$. The boundary conditions were velocity inlet, pressure outlet, and wall boundary. The values of $\rho = 1.225$ kg/m^3, $\mu = 1.79 \times 10^{-5}$ Pa s and Tu = 0.1 % were used for air density and air dynamic viscosity and free stream turbulence (Selig et al. 1995). The c-type structured grids for the 2D airfoil were created using the GAMBIT software as shown in Fig. 2a. Because of the computational demand, the grid independence study is limited to the 2D case for angles of attack of 6° and 10°, including the lift and drag coefficients.

In the 3D case, only the k–k_L–ω transition model was used. For the boundary conditions, it is noted that the wind tunnel walls were ignored, and computations of a free turbine blade were carried out. Only one of the turbine blades was explicitly modeled in the computations, exploiting the 120° symmetry of the three-bladed turbine. The simulation used the moving reference frame (MRF) function of FLUENT^{TM} to simplify the assumptions of steady-state flow conditions. Like 2D simulation, boundary conditions such as the velocity inlet, pressure outlet, and viscous wall boundary were considered. The values of the air density and air dynamic viscosity are identical to the 2D simulation. A free stream turbulence intensity was chosen as Tu = 0.35 %, which is same as the wind tunnel experiment performed in this study. The grid was generated using GAMBIT^{TM} and was divided into three parts: first, the boundary layer flow region is around the turbine blade in order to resolve the transitional boundary layer, and the wall coordinate y+ of the first point away from the wall surface was set to be 1 based on the 2D grid system. Next, the inner flow region is composed of the unstructured grids with the triangle elements. Finally, the outer flow region extends to the three sides of the inner flow region with the structured grids. The mesh domain of the 3D turbine blade is shown in Fig. 2b. The total cell numbers of 3D simulation are 3,509,920. The 3D simulation results of the mechanical power were compared with the experimental data obtained from the wind tunnel experiments.

Results and discussion

In our previous work (Bai and Hsiao 2010; Hsiao et al. 2013), an in-house code for predicting the aerodynamic performance of a HAWT was developed. This code utilizes 2D airfoil data to calculate the sectional aerodynamic loads of the turbine blade along with the modified axial and angular induction factors. In this study, the simulation code was also used to calculate the distributions of the angles of

attack in each blade section between the TSR of 2 and 7 at the wind speed of 10 m/s as shown in Fig. 3.

2D validation

Different-sized grids with 14500, 28500, 31800, 48300, and 52000 cells were examined to ensure the grid independence of the numerical results, which were compared with the experimental data obtained from wind tunnel test (Selig et al. 1995). The comparison between numerical and experimental results at angle of attack of 10° and Reynolds number of 1×10^5 is presented in Table 2. It can be seen that, with the various grid sizes, the relative errors of the lift and drag coefficients are within reasonable range. Therefore, the grid size with 31,800 cells was selected for all 2D computational domain.

To resolve the boundary layers, the height of the first layer of the grid around the airfoil surface was set to be 1.75×10^{-5} m, corresponding to $y+ = 1$. For this reason, the results of lift and drag coefficients for the SD8000 airfoil at the angle of attack of 10° were examined using the k–k_L–ω and γ–$Re_{\theta t}$ transition models presented in Table 3. By comparing with experimental data (Selig et al. 1995), k–k_L–ω transition model provides more accurate prediction for lift and drag coefficients.

Observation of streamline on the upper side of the airfoil was also implemented via both models at the angle of attack of 10° and $y+ = 1$, as shown in Fig. 4. It can be seen clearly from the k–k_L–ω transition model results (Fig. 4a) that the LSB characteristics including separation and reattachment points occurred close to leading edge. On the other hand, in the results obtained from γ–$Re_{\theta t}$ transition model (Fig. 4b), no LSB was found on the surface of

the blade. According to the published literatures, a LSB should form at this Reynolds number (Genç et al. 2009, 2011, 2012; Menter et al. 2004; O'Meara and Mueller 1987). Therefore, we concluded that the prediction of flow characteristics on the upper surface using the k–k_L–ω transition model is closer to the real flow condition.

Figure 5 shows the lift and drag coefficient variation with angles of attack for the 2D simulation. The simulation results are compared with the experimental data obtained from wind tunnel experiments (Selig et al. 1995). The numerical results for the steady-state flow from the k–k_L–ω transition model and the γ–$Re_{\theta t}$ transition model were also shown in Fig. 5. It can be seen that both models for the lift coefficient gave reasonable agreement with the experimental data between the angles of attack of −6° and 1°. At angles of attack between 1° and 2°, the lift coefficients presented in the experiments increased suddenly. It seems that the LSB formed at the angle of attack of 2° (O'Meara and Mueller 1987). Therefore, a slight error for predicting lift coefficient occurred between the angles of attack of 2° and 10° with the γ–$Re_{\theta t}$ transition model. The lift coefficient is successfully captured at those of angles of attack using the k–k_L–ω transition model. As the curve of lift coefficients goes to the stall region ($\alpha = 11°$–20°), the γ–$Re_{\theta t}$ transition model fails to predict the lift coefficient. The trend of the lift coefficient in the stall region was predicted well via the k–k_L–ω transition model, but the simulation results were slightly higher than the experimental data. The transient simulation results from k–k_L–ω transition model were almost identical with the ones in steady-state flow at the angles of attack between 11° and 20°.

The discussions on drag curves are divided into three parts: first, at the angles of attack between −6° and 4°, the errors for predicting drag coefficients were within 10 % for both numerical models. Second, the simulation results within the angles of attack of 5° and 14° do not match the experimental data through the k–ω SST turbulence model, but the results from the k–k_L–ω transition model still gave good agreement with the experimental data. Finally, both models fail to predict the drag curves in the stall region. According to the experimental data, after the angle of attack of 15°, there is a discontinuity on the drag coefficient curve, which is difficult to be predicted without particular user-defined function (Genç et al. 2009, 2011). As with the lift coefficient predictions, the drag values obtained via k–k_L–ω transition model for the transient flow were almost the same as the ones for steady-state flow at the angles of attack between 11° and 20°.

Experimental results

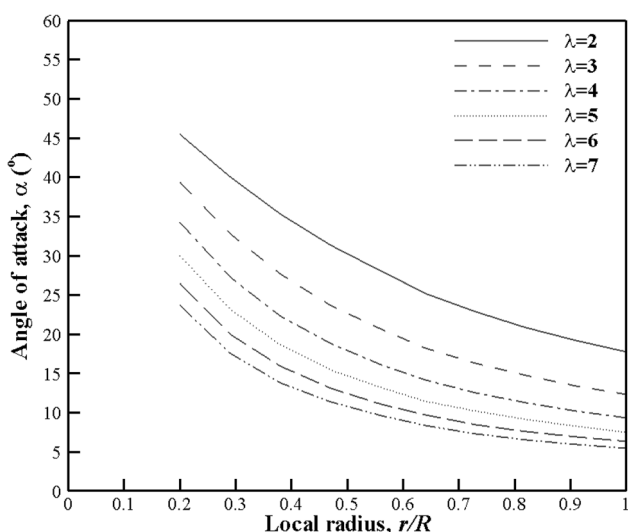Figure 6 shows the variation of mechanical power with respect to the TSR between 0 and 7 at the wind speed of

Fig. 3 Distributions of angles of attack in each blade section between tip speed ratios of 2 and 7 at wind speed of 10 m/s

Table 2 Comparison of simulation and experimental results for grid independence study

Cases	C_l	C_l relative error (%)	C_d	C_d relative error (%)
14,500 Cells	1.376	25.1	0.0688	49.6
28,500 Cells	1.222	11.1	0.0544	18.3
31,800 Cells	1.065	3.2	0.0459	0.2
48,300 Cells	1.066	3.1	0.0461	0.2
52,000 Cells	1.065	3.2	0.0459	0.2
Experiment	1.100		0.046	

Table 3 Evaluation of the features of the two turbulence models for 2D SD8000 airfoil at the angle of attack of 10°

$\alpha = 10°$	C_l	Error (%)	C_d	Error (%)
Experiment data	1.10		0.046	
$k–k_L–\omega$	1.065	3.2	0.0459	0.2
$\gamma–Re_{\theta t}$	1.006	8.6	0.0527	14.5

10 m/s obtained from the simulation and the wind tunnel experiments. The values of mechanical power increased with TSR from 0 to 5.5, at which the maximum mechanical power was 117 W. After TSR of 5.5, the mechanical power decreased to 75.8 W with TSR of 6.8. It is known from Fig. 1 that the turbine blades operate at very high angles of attack from TSR of 2 to 5 at the wind speed of 10 m/s. The turbine blade produces less mechanical power when it operates at the stall region. The mechanical power starts decreasing from TSR of 5.8 as the L/D ratio begins decreasing.

CFD simulation results

Power production

All 3D simulations were implemented by the $k–k_L–\omega$ transition model. Due to the steady-state flow conditions in the MRF, the 3D simulation cases can be implemented by the $k–k_L–\omega$ transition model with the state-steady flow. The results of mechanical torque were obtained with TSR of 2–7 at wind speed of 10 m/s. The values of mechanical torque can be converted to mechanical power for comparing with the experimental data by

$$P_m = T_m\omega, \tag{4}$$

where the ω is rotational speed and T_m is the mechanical torque.

The comparison of experimental and simulation results are shown in Fig. 7. Note that the comparison at TSR of 7 was made with an extrapolation of the experimental power curve.
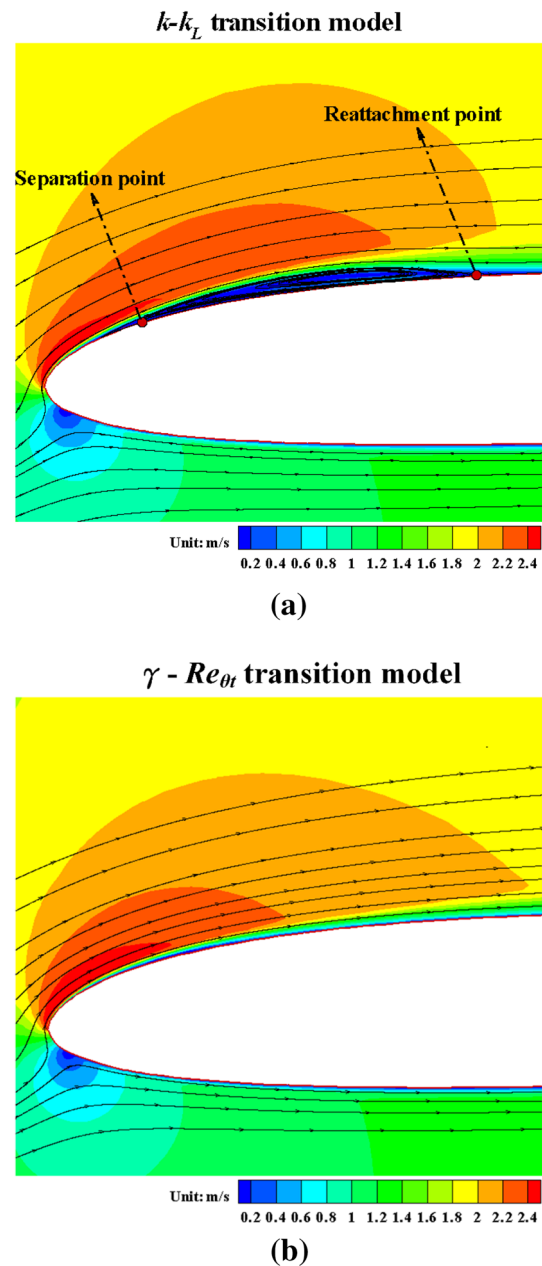

Fig. 4 Velocity magnitude contour on the 2D SD8000 airfoil at 10° angle of attack **a** $k–k_L–\omega$ transition model and **b** $\gamma–Re_{\theta t}$ transition model. *Streamlines* are also shown on the *contour plots*
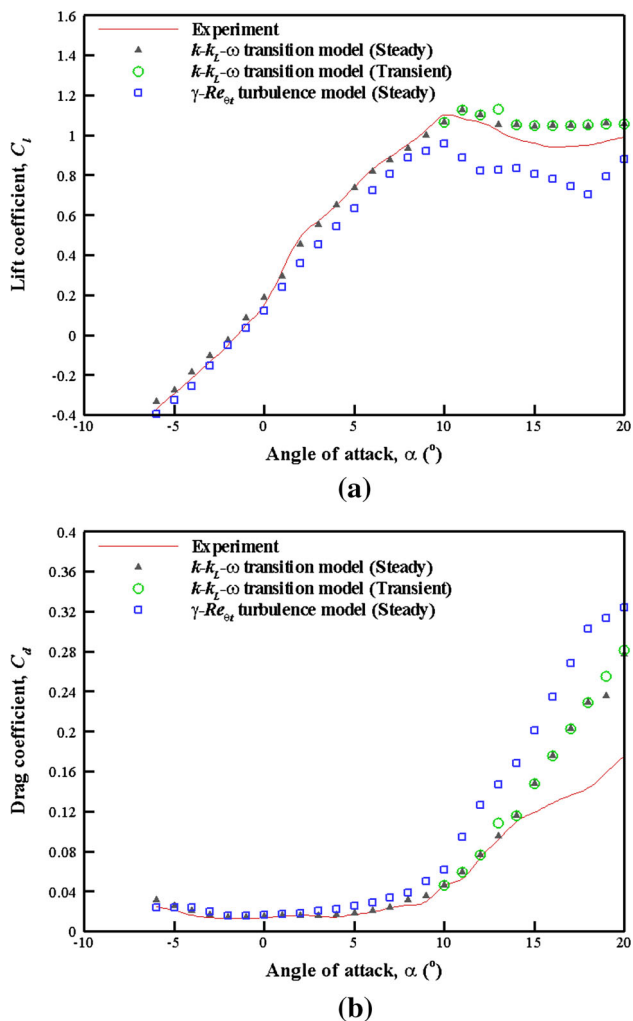
Fig. 5 Numerical and experimental results for the **a** lift and **b** drag coefficients of the SD8000 airfoil at Reynolds number of 1×10^5

Fig. 6 Comparison of mechanical power values obtained from experiments and simulations at wind speed of 10 m/s

It can be seen clearly from Fig. 6 that the simulation results of the mechanical power have a good agreement with the experimental data at TSRs of 4, 5, 6, and 7, and these cases will be further examined with regard to laminar separation. The simulation results at TSRs of 2 and 3 are slightly higher than the experimental data. Because the turbine blade was operating at the stall region ($\alpha = 18°$–$45°$) with the transient effects in flow field, the flow was fully separated on the upper blade surface. The flow condition becomes unsteady, and it is difficult to make precise predictions within this region.

Flow characteristics around the blades

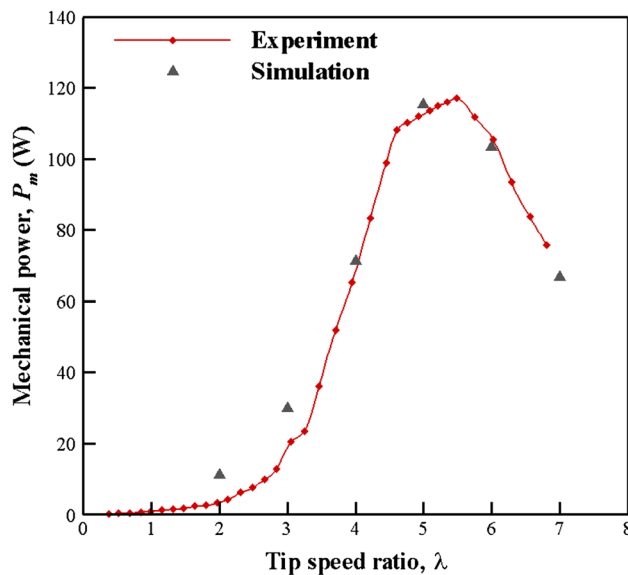Figure 7 displays the skin friction lines on the suction surface of the turbine blade at various TSRs. The phenomenon of laminar separation, including separation and reattachment, was clearly observed on the blade surface at the TSRs between 4 and 7. The radial flows move toward trailing edge before the separation line. The recirculating flows move from reattachment line to separation line. Combination of the radial and recirculating flow generates a vortex in the separation region (Herráez et al. 2014), and this vortex results in the pressure difference on the blade surface at certain rotational speed and makes the fluid particles diffuse from the turbine blade root to the tip. At TSR of 4, the flow separated along the leading edge at the range between $r/R = 0.82$ and 0.20. With the increasing TSR from 4 to 7, the separation lines gradually moved to the trailing edge from the leading edge. When TSR reached to 7, the separation line was almost at 70 % chord length of the tip region, and the range of leading edge separation is reductive between $r/R = 0.2$ and 0.25.

Observations of the reattachment lines shown in Fig. 7 can be divided into two parts: first, the attachment line moves backward to the trailing edge with increasing TSR between $r/R = 0.56$ and 1.0. At the TSRs of 6 and 7, the attachment lines were close to the trailing edge. At the local radius between $r/R = 0.20$ and 0.56, the reattachment lines gradually move toward leading edge with increasing TSR. As TSR increases, the reattachment lines seem to be pushed to the trailing edge by the moving separation lines at the local radius from $r/R = 0.47$ to 0.95. It is concluded that the laminar separation was pushed to the trailing edge while increasing TSR at the tip region of the blade. This phenomenon can be attributed to the stronger tip vortex when TSR is increased. The tip region is affected as angle of attack was reduced.
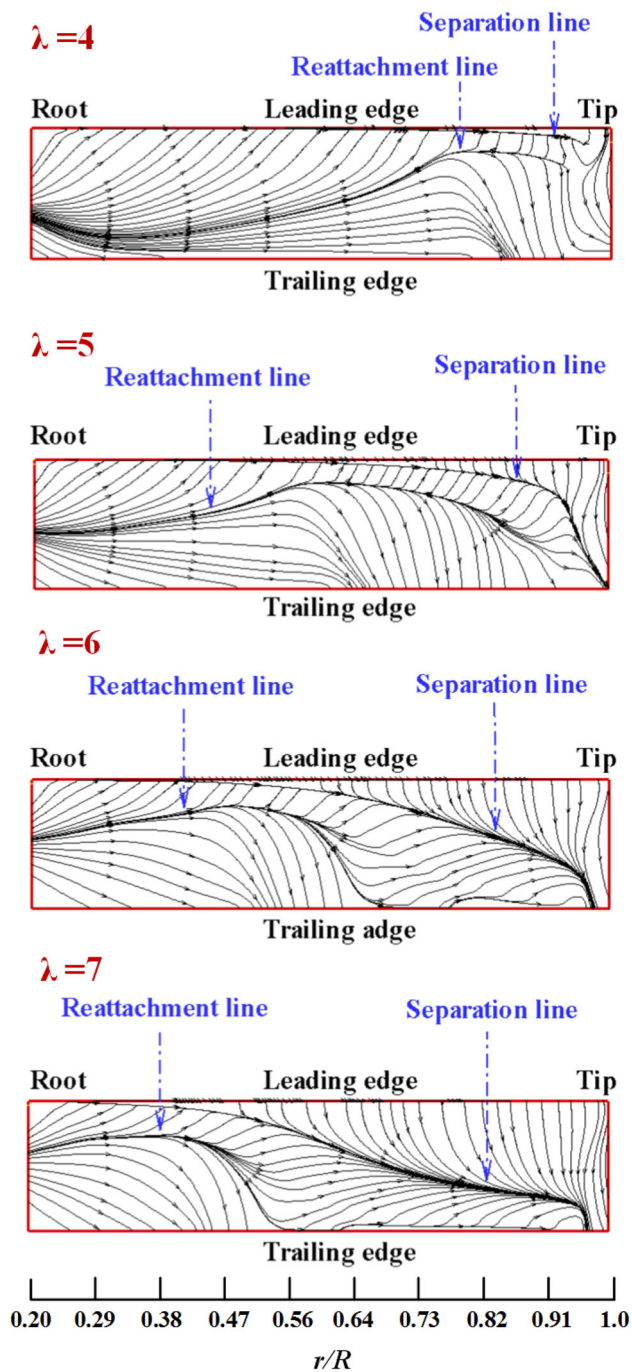
Fig. 7 Limiting streamline distributions on the turbine blade suction surface at wind speed of 10 m/s

Figure 8 shows the streamlines passing over the 2D airfoil and the 3D blade section performed at TSR of 6. Three blade sections, including $r/R = 0.91$, 0.47, and 0.29 with the angles of attack of 20°, 13°, and 7°, respectively, are displayed for the observation of laminar separation. The angles of attack for 3D blade sections were computed using BEMT method (Hsiao et al. 2013), which calculates the angles of attack in each section by iterating the axial induction factor and angular induction factor. As shown in Fig. 8a, the laminar separation at the local blade section of $r/R = 0.91$ is close to the trailing edge. Comparing to the 3D simulation, the position of the laminar separation on 2D airfoil is near the leading edge. Since the 3D analysis is simulating the rotating turbine blade, the centrifugal force acting on the separated flow, which is proportional to the square of rotational speed, becomes the largest contributor for this position difference (Herráez et al. 2014). At the local blade section of $r/R = 0.47$, as shown in Fig. 8b, the separation point is located at the leading edge for 2D airfoil but moves to approximately 10 % chord length from the leading edge for 3D blade. As the angle of attack was increased to 20° ($r/R = 0.29$), fully separation occurred for 2D airfoil and the laminar separation existed closer to the leading edge compared to the previous cases, as shown in Fig. 8c. The laminar separation moving from leading edge to trailing edge with the increase of blade radius also results from the effect of centrifugal force (Chaviaropooulos and Hansen 2000; Herráez et al. 2014). This effect also reduces the size of LSB from the 2D analysis to the 3D one. In addition, the Coriolis force which acts on radial flow leads to the laminar separation toward trailing edge. These effects result in delay of separation on the suction surface of the blade.

Figure 9 presents the locations of the separation points on the suction surface of the 2D airfoil and 3D turbine blade at the TSR of 6 and at the angles of attack of 7°, 13°, and 20°. The non-dimensionalized chord length, $c_r/c = 0$, represents the leading edge and $c_r/c = 1$ represents the trailing edge, where c_r is the local chord length and c is the chord length. It is shown that the separation points move toward leading edge with the increase of angle of attack. For the 3D analysis, the separation point is near to the trailing edge ($c_r/c = 0.67$) at the angle of attack of 7°. All the locations of separation points in the 3D analysis are different from the 2D analysis due to the centrifugal force from the rotating behavior.

Conclusions

This study investigates the laminar separation at the upper surface of a rotating HAWT blade numerically and experimentally. Firstly, the agreement of 2D simulation with experimental data for the prediction of lift and drag coefficients of SD8000 airfoil suggests that the k–k_L–ω transition model is an appropriate choice for observing laminar separation on 3D turbine blade. Second, the 3D CFD simulation agreed well with wind tunnel experiment at the TSRs from 4 to 7 and at the wind speed of 10 m/s, and the maximum mechanical power was measured to be 117 W at the TSR of 5.5. The observation of the separation

Fig. 8 The investigations of laminar separation on the turbine blade suction surface at **a** $r/R = 0.91$, **b** $r/R = 0.47$, and **c** $r/R = 0.29$ and the 2D airfoil

(a)

(b)

(c)
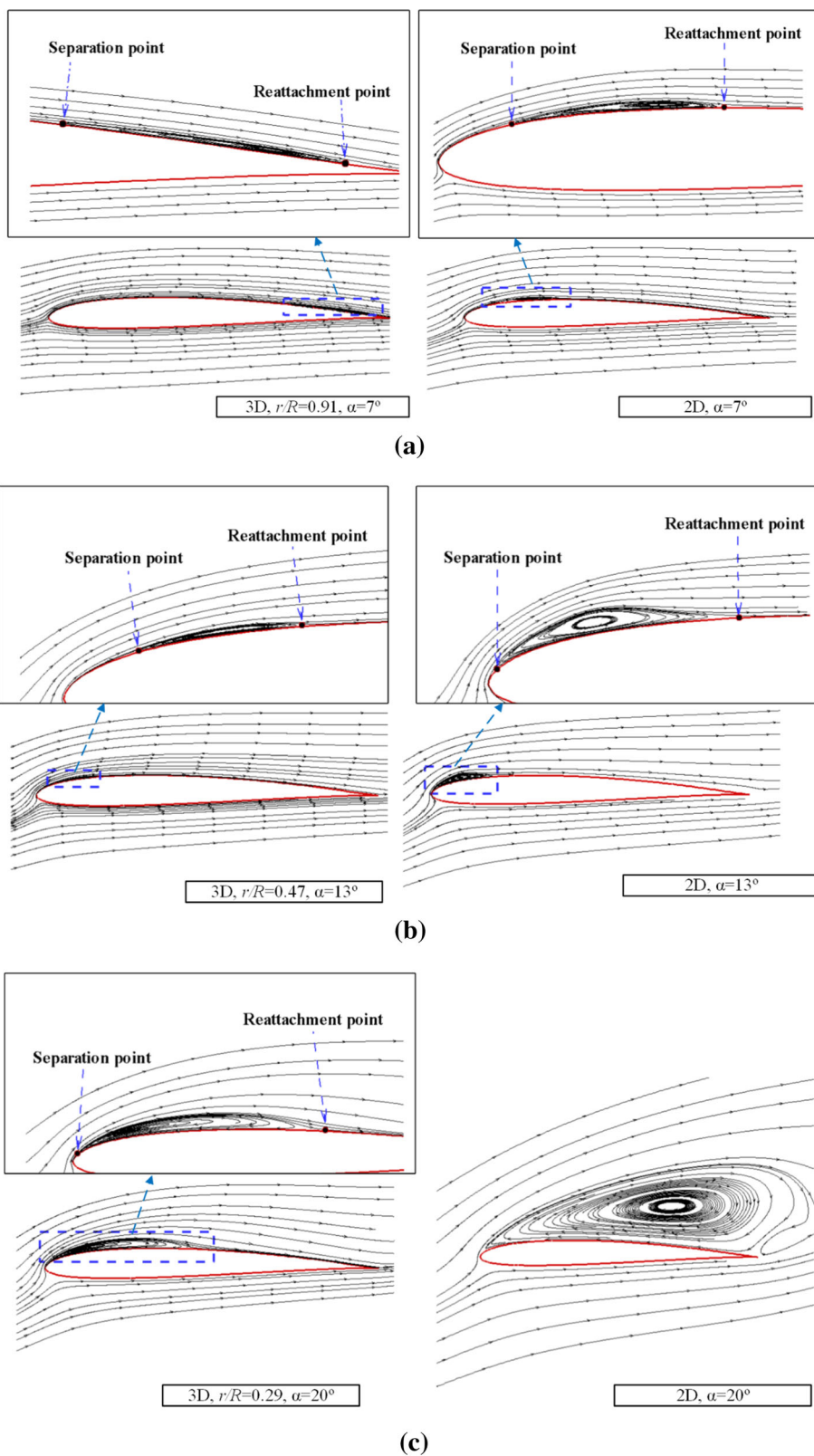
and reattachment lines on the suction surface of the turbine blade at various TSRs reveals that the laminar separation moves toward the trailing edge with the increasing TSR in the blade tip region. In addition, the vortex generated by the radial and recirculating flow in the separation region results in the pressure difference on the surface of the blade
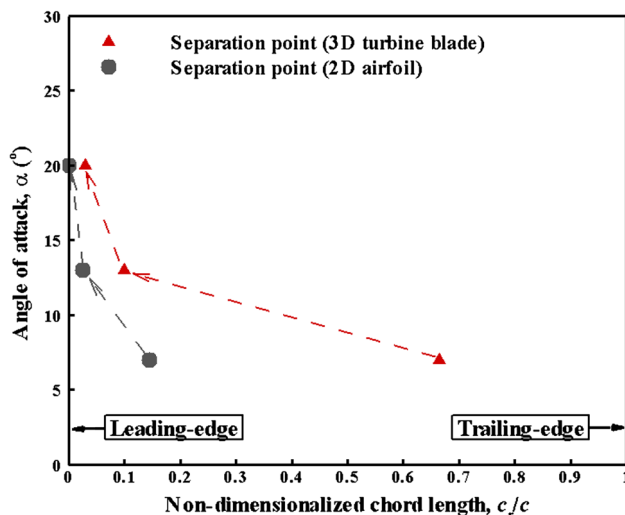
Fig. 9 Locations of separation points in 2D airfoil and 3D turbine blade at the TSR of 6 and wind speed of 10 m/s and at the angles of attack of 7°, 13°, and 20°

and forces the flow to diffuse from the blade root to the tip. It can be clearly seen that the laminar separation occurred on the rotating turbine blade through the observation of the streamlines passing over 2D airfoil and 3D blade sections. Due to the contribution of the centrifugal force, the LSB moves from leading edge to trailing edge with the increase of blade radius, and this also results in the delay of separation on the suction surface of the blade at each local radius.

References

Bai CJ, Hsiao FB (2010) Code development for predicting the aerodynamic performance of a HAWT blade with variable-operation and verification by numerical simulation. Paper presented at the 17th National Computational Fluid Dynamics Conference, Taoyuan, Taiwan, July 2010

Bai C-J, Wang W-C, Chen P-W, Chong W-T (2014) System integration of the horizontal-axis wind turbine: the design of turbine blades with an axial-flux permanent magnet generator. Energies 7:7773

Bai C-J, Chen P-W, Wang W-C (2016) Aerodynamic design and analysis of a 10 kW horizontal-axis wind turbine for Tainan. Taiwan Clean Technol Environ Policy 18:1151–1166. doi:10.1007/s10098-016-1109-z

Bassi F, Crivellini A, Rebay S, Savini M (2005) Discontinuous Galerkin solution of the Reynolds-averaged Navier–Stokes and k–ω turbulence model equations. Comput Fluids 34:507–540. doi:10.1016/j.compfluid.2003.08.004

Bechmann A, Sørensen NN, Zahle F (2011) CFD simulations of the MEXICO rotor. Wind Energy 14:677–689. doi:10.1002/we.450

Byerley AR, Störmer O, Baughn JW, Simon TW, Van Treuren KW, List J Jr (2003) Using Gurney flaps to control laminar separation on linear cascade blades. J Turbomach 125:114–120. doi:10.1115/1.1518701

Chaviaropooulos PK, Hansen MOL (2000) Investigating three-dimensional and rotational effects on wind turbine blades by means of a quasi-3D Navier–Stokes solver. J Fluids Eng 122:330–336

Digraskar DA (2010) Simulations of flow over wind turbines. Master Thesis, Department of Mechanical and Industrial Engineering, University of Massachusetts, Amherst

Genç MS, Kaynak U, Lock GD (2009) Flow over an aerofoil without and with a leading-edge slat at a transitional Reynolds number. Proc Inst Mech Eng G 223:217–231. doi:10.1243/09544100JAERO434

Genç MS, Kaynak Ü, Yapici H (2011) Performance of transition model for predicting low Re aerofoil flows without/with single and simultaneous blowing and suction. Eur J Mech B 30:218–235. doi:10.1016/j.euromechflu.2010.11.001

Genç MS, Karasu İ, Hakan Açıkel H (2012) An experimental study on aerodynamics of NACA2415 aerofoil at low Re numbers. Exp Therm Fluid Sci 39:252–264. doi:10.1016/j.expthermflusci.2012.01.029

Herráez I, Stoevesandt B, Peinke J (2014) Insight into rotational effects on a wind turbine blade using Navier–Stokes computations. Energies 7:6798

Hirahara H, Hossain MZ, Kawahashi M, Nonomura Y (2005) Testing basic performance of a very small wind turbine designed for multi-purposes. Renew Energy 30:1279–1297. doi:10.1016/j.renene.2004.10.009

Hsiao F-B, Bai C-J, Chong W-T (2013) The performance test of three different horizontal axis wind turbine (HAWT) blade shapes using experimental and numerical methods. Energies 6:2784–2803. doi:10.3390/en6062784

Huang J, Corke TC, Thomas FO (2006) Unsteady plasma actuators for separation control of low-pressure turbine blades. AIAA J 44:1477–1487. doi:10.2514/1.19243

Kang HS, Meneveau C (2010) Direct mechanical torque sensor for model wind turbines. Meas Sci Technol 21:1–10. doi:10.1088/0957-0233/21/10/105206

Langtry R, Janusz G, Florian M (2006) Predicting 2D airfoil and 3D wind turbine rotor performance using a transition model for general CFD codes. In: 44th AIAA aerospace sciences meeting and exhibit. Aerospace sciences meetings. American Institute of Aeronautics and Astronautics. doi:10.2514/6.2006-395

Lian Y, Shyy W (2007) Laminar–turbulent transition of a low Reynolds number rigid or flexible airfoil. AIAA J 45:1501–1513. doi:10.2514/1.25812

Malan P, Suluksna K (2009) Calibrating the gamma-Re_theta transition model for commercial CFD. In: The 47th AIAA aerospace sciences meeting, Orlando, Florida, January 2009

Menter FR (1994) Two-equation eddy-viscosity turbulence models for engineering applications. AIAA J 32:1598–1605. doi:10.2514/3.12149

Menter FR, Langtry RB, Likki SR, Suzen YB, Huang PG, Völker S (2004) A correlation-based transition model using local variables—Part I: model formulation. J Turbomach 128:413–422

O'Meara M, Mueller TJ (1987) Laminar separation bubble characteristics on an airfoil at low Reynolds numbers. AIAA J 25:1033–1041. doi:10.2514/3.9739

Pape AL, Lecanu J (2004) 3D Navier–Stokes computations of a stall-regulated wind turbine. Wind Energy 7:309–324. doi:10.1002/we.129

Richards PJ, Hoxey RP (1993) Appropriate boundary conditions for computational wind engineering models using the k–ε turbulence

model. J Wind Eng Ind Aerodyn 46–47:145–153. doi:10.1016/0167-6105(93)90124-7

Rist U, Maucher U (2002) Investigations of time-growing instabilities in laminar separation bubbles. Eur J Mech B 21:495–509

Schlichting H, Gersten K (2003) Boundary layer theory, 8th edn. Springer, Berlin

Selig MS, McGranahan BD, Broughton BA (1995) Summary of low-speed airfoil data. SoarTech Publications, Virginia Beach

Shan H, Jiang L, Liu C (2005) Direct numerical simulation of flow separation around a NACA 0012 airfoil. Comput Fluids 34:1096–1114. doi:10.1016/j.compfluid.2004.09.003

Sharma DM, Poddar K (2010) Investigations on quasi-steady characteristics for an airfoil oscillating at low reduced frequencies. Int J Aerosp Eng 2010:1–11. doi:10.1155/2010/940528

Shih T-H, Liou WW, Shabbir A, Yang Z, Zhu J (1995) A new k–ε eddy viscosity model for high Reynolds number turbulent flows. Comput Fluids 24:227–238. doi:10.1016/0045-7930(94)00032-T

Singh NK, Sarkar S (2011) DNS of a laminar separation bubble. World Acad Sci Eng Technol 5:403–407

Spera DA (1994) Wind turbine technology: fundamental concepts of wind turbine engineering. ASME Press, New York

Stapleton KW, Guentsch E, Hoskinson MK, Finlay WH (2000) On the suitability of k–ε turbulence modeling for aerosol deposition in the mouth and throat: a comparison with experiment. J Aerosol Sci 31:739–749. doi:10.1016/S0021-8502(99)00547-9

Swanson TA, Isaac KM (2010) Planform and camber effects on the aerodynamics of low-Reynolds-number wings. J Aircr 47:613–621. doi:10.2514/1.45921

Walters DK, Leylek JH (2004) A new model for boundary layer transition using a single-point RANS approach. J Turbomach 126:193–202